Structure of Polymer-Grafted Nanoparticle Melts

Jiarul Midya[†], **Michael Rubinstein**[‡], **Sanat K. Kumar**[¶], **Arash Nikoubashman**[*,†]

[†]Institute of Physics, Johannes Gutenberg University Mainz, Staudingerweg 7, 55128 Mainz, Germany

[‡]Department of Mechanical Engineering and Materials Science, Biomedical Engineering, Chemistry, and Physics, Duke University, Durham, NC 27708-0300, USA

[¶]Department of Chemical Engineering, Columbia University, New York, New York 10027, USA

Abstract

The structure of neat melts of polymer-grafted nanoparticles (GNPs) is studied *via* coarse-grained molecular dynamics simulations. We systematically vary the degree of polymerization and grafting density at fixed NP radius, and study in detail the shape and size of the GNP coronas. For sufficiently high grafting density, chain sections close to the NP core are extended and form a dry layer. Further away from the NP there is an interpenetration layer, where the polymer coronas of neighboring GNPs overlap and the chain sections have almost unperturbed conformations. To better understand this partitioning, we develop a two-layer model, representing the grafted polymer around a NP by spherical dry and interpenetration layers. This model quantitatively predicts that the thicknesses of the two layers depend on one universal parameter, x, the degree of overcrowding of grafted chains relative to chains in the melt. Both simulations and theory show that the chain extension free energy is non-monotonic with increasing chain length at fixed grafting density, with a well defined maximum. This maximum is indicative of the crossover from the dry layer-dominated to interpenetration layer-dominated regime, and it could have profound consequences on our understanding of a variety of anomalous transport properties of these GNPs. Our theoretical approach therefore provides a facile means for understanding and designing solvent-free GNP-based materials.

Graphical TOC Entry

[*]To whom correspondence should be addressed anikouba@uni-mainz.de, jimidya@uni-mainz.de.

[1]In an FCC configuration, a cubic unit cell with edge length $2\sqrt{2}R$ is occupied by four spheres with radius R (eight 1/8 spheres at the eight corners and six hemispheres at the six faces). Thus, $V_{\text{void}} = (2\sqrt{2}R)^3 - 16\pi R^3/3 = 8(\sqrt{8} - 2\pi/3)R^3$.

Simulation   Two-layer model
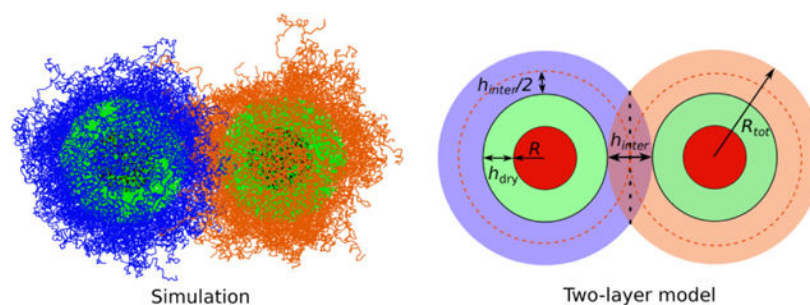
Over the past few decades, polymer nanocomposites have gained significant attention due to their wide range of applications in drug delivery,[1–3] desalination,[4–6] photonic,[7,8] and phononic materials.[9,10] These applications often require a homogeneous dispersion of nanoparticles (NPs) in the polymer matrix to optimize their physical properties. In practice, however, such uniform mixing is difficult to achieve, due to the chemical incompatibility between the two components. Instead, one often encounters undesired aggregation of the (inorganic) NPs in the (organic) polymer matrix, which can lead to deterioration of material properties and mechanical stability of the composite. Such phase separation can be prevented by grafting the polymers on the surface of the NPs, *i.e.*, turning these two component systems into effectively one component systems.[11–19] These hybrid particles, known as polymer-grafted NPs (GNPs) or hairy NPs, typically exhibit a core-shell morphology with a hard core and a soft corona. While many previous theoretical descriptions focused on GNPs mixed with small molecule solvents,[20,21] we are interested in melts of GNPs where the surrounding medium is composed of other GNPs. This situation has received significantly less theoretical attention to date.[22–25]

The hybrid nature of GNPs can substantially improve, *e.g.*, the mechanical,[26–33] optical,[34,35] thermal,[36,37] electrical,[36,37] and rheological[38,39] properties of a material in comparison to the corresponding bulk polymer or traditional physically mixed NP/polymer composites. These properties are controlled by the grafting density of the chains and their degree of polymerization, the size and shape of the cores, the interactions between the polymers and the cores, *etc*. For example, the elastic moduli of GNP systems can be tuned by varying the NP loading through the grafting density and/or the length of the grafted polymers. Even at fixed NP loading, the mechanical properties of GNPs depend on their microscopic details, as was demonstrated in recent experiments and simulations.[30] In that work, significant deviations of the elastic moduli were observed compared to predictions based on a simple mean-field description,[40] with sparsely grafted GNP systems exhibiting higher elastic moduli compared to densely grafted GNPs.[30] This enhancement was attributed to the coil-like conformations of the sparsely grafted chains, which promoted a higher degree of polymer interpenetration compared to densely grafted NPs with short chains. It is thus clear that the microscopic details of GNPs play an important role in their macroscopic material properties.

In previous experiments and simulations, the phase behavior of GNPs in neat melts or within polymer matrices was studied.[41–47] It was found, *e.g.*, that GNPs in such solvent-free conditions exhibit structural transitions from a simple liquid to a glass forming liquid, or

from star-polymer-like to colloid-like behavior with variations of grafted polymer length and grafting density.[42,44,47] Recent field-based simulations have shown that GNPs in a homopolymer matrix exhibit an entropically driven mixing-demixing transition,[46] which was controlled by the core size and the ratio of the lengths of the free and grafted polymers. In the demixed state, the GNPs self-assembled into a variety of nanostructures, such as sheets, wires, and capsules, depending on, *e.g.*, the size and shape of the NPs, grafting density, length of the grafted polymers, and intermolecular interactions.[48–50] However, to date, there is only a small number of studies on pure GNP melts that focus on the size, shape, and interpenetration of the polymer coronas of the GNPs on a microscopic level. Understanding these aspects could elucidate a variety of anomalous transport properties of these GNP systems.[51]

To fill this void, we investigate the structure of neat melts of GNPs *via* coarse-grained molecular dynamics (MD) simulations. We systematically vary the degree of polymerization and grafting density at fixed NP core radius, and study in detail the shape, size, and interpenetration of the polymer coronas surrounding the NP cores. Further, we analyze the conformations of the grafted polymers and compare them with their pure bulk polymer analogs to assess both the effects of chain grafting and of the presence of other GNPs. To rationalize our simulation results, we introduce a two-layer model, in which the polymer corona is divided into a dry layer, *i.e.*, the region where only few monomers from surrounding GNPs were present, and an interpenetration layer, which is characterized by a significant overlap between grafted chains of surrounding GNPs. Sections of grafted chains belonging to the dry layer are extended, whereas parts in the interpenetration layer are almost unperturbed. This model predicts that the thicknesses of the two layers depend on a single parameter, which essentially describes the degree of overcrowding of grafted chains compared to unperturbed chains in a melt. The analytical predictions for the thicknesses of the dry and interpenetration layers are in excellent quantitative agreement with our simulation results across a broad parameter range with the use of a single adjustable constant.

Two-Layer Model

In our theoretical model, the grafted layer of a GNP consists of a dry and an interpenetration layer with thicknesses h_{dry} and h_{inter}, respectively [see the schematic shown in Fig. 1 (a)]. To estimate the overall brush thickness of the GNPs, $h = h_{dry} + h_{inter}/2$, we consider a single isolated GNP with a spherical polymer brush. In this case, the volume of the spherical shell between R and $R + h$ is completely occupied by all monomers from the grafted chains, and the brush thickness is simply given by the space-filling condition

$$\frac{4}{3}\pi\left[(R + h)^3 - R^3\right] = Z\frac{N}{\rho} \tag{1}$$

where R is the radius of the NP, $Z = 4\pi R^2 \rho_g$ is the number of chains grafted to the NP with grafting density ρ_g, N is the number of Kuhn monomers per grafted chain, and ρ is the Kuhn monomer number density (assumed uniform) within the spherical shell. Thus, the total radius of the GNP is:

$$R_{\text{tot}} = \left(R^3 + \frac{3ZN}{4\pi\rho}\right)^{1/3} \tag{2}$$

and the brush thickness is given by

$$h = R_{\text{tot}} - R = \left(R^3 + \frac{3ZN}{4\pi\rho}\right)^{1/3} - R. \tag{3}$$

This estimate for h ignores that the actual shape of the polymer layers at dense packing must correspond to the Voronoi cells defined by the position of the NPs, *e.g.*, a rhombic dodecahedron for the face-centered cubic (FCC) packing of spheres [see Fig. 1(b)]. In the simulations, the brush thickness h can be defined in various ways (see Simulations section and ESI for details). The resulting values for h are all within 5–10% of each other, and they all vary similarly with the parameters of the system N and Z (see Table 1). In our simulations, we chose the radially averaged center of the interpenetration layer to determine the brush thickness, and we can match the theoretical predictions by introducing an empirical shape factor $a \approx 0.93$, that reduces all theoretical curves for h, h_{dry} and h_{inter} [see Eqs. (3), (8) and (10)] by 7%.

Next, we discuss the interpenetration between the polymer coronas from neighboring GNPs using the two-layer model. This model assumes that the dry and interpenetration layers are spherical, and that the overlap between neighboring GNPs is primarily pairwise. If we further posit that, on average, each grafted chain has $n_{\text{dry}} = N - n_{\text{inter}}$ Kuhn monomers in the dry layer and the remaining n_{inter} monomers in the interpenetration layer, then the space-filling condition for the dry layer can be rewritten by analogy with Eq. (1)

$$\frac{4}{3}\pi\left[\left(R + h_{\text{dry}}\right)^3 - R^3\right] = Z\frac{n_{\text{dry}}}{\rho}. \tag{4}$$

An analogous expression can be formulated for the interpenetration layer, which is equally shared between neighboring GNPs, by replacing in Eq. (1) h with $h_{\text{inter}}/2$, and R with $R + h_{\text{dry}}$

$$\frac{4}{3}\pi\left[\left(R + h_{\text{dry}} + h_{\text{inter}}/2\right)^3 - \left(R + h_{\text{dry}}\right)^3\right] = Z\frac{n_{\text{inter}}}{\rho}. \tag{5}$$

Here, we have assumed that all grafted chains enter the interpenetration layer which is corroborated by our simulations, where 98% to 100% of the grafted chains had at least one bead in the interpenetration layer. We can solve Eqs. (4) and (5) under the assumption that the chain sections in the interpenetration layer are unperturbed with root-mean-square end-to-end distance

$$h_{\text{inter}} = bn_{\text{inter}}^{1/2} \tag{6}$$

where b is the Kuhn length of the polymer. It is important to note that we can combine Eqs. (4) and (5), and then the result for $h_{\text{dry}} + h_{\text{inter}}/2$ is identical to the result for h [see Eq. (3)].

A detailed derivation of the analytical solution of the two-layer model is provided in the ESI, and below we will focus on its key results. The main parameter of our analytical solution is

$$x = \frac{Z}{\pi \rho b^2 R_{\text{tot}}} = \frac{Z}{\pi \rho b^2 \left[R^3 + 3ZN/(4\pi\rho) \right]^{1/3}} \tag{7}$$

which monotonically decreases with increasing N at fixed Z, and monotonically increases with increasing Z at fixed N. To understand the physical basis of this parameter, we consider a volume R_{tot}^3 in an unperturbed polymer melt. This volume is occupied by $\rho R_{\text{tot}}^3 / N_{\text{tot}}$ chains, where N_{tot} is defined through the equation $R_{\text{tot}}^2 = N_{\text{tot}} b^2$. The number of chains that fill this volume in an unperturbed melt is on the order of $\rho b^2 R_{\text{tot}}$, and therefore x is proportional to the ratio of the actual number of graft chains Z to the number of chains that occupy the same volume in an unperturbed melt. Hence, $x \approx \mathcal{O}(1)$ corresponds to an (almost) unperturbed melt, whereas $x \gg 1$ implies that the volume is overcrowded and the grafted chains are strongly extended.

We can write the analytical solution for h_{inter} using the parameter x as

$$h_{\text{inter}} = 3R_{\text{tot}}(1 + x)\left[1 - \sqrt{1 - \frac{4}{3}\left(\frac{1}{1 + x}\right)^2} \right]. \tag{8}$$

The volume fraction of the interpenetration layer in the GNP system, $\phi_{\text{inter}} = (Zn_{\text{inter}}/\rho)/\left(4\pi R_{\text{tot}}^3 /3\right)$, is then given by

$$\phi_{\text{inter}} = \frac{27}{4}x(1 + x)^2\left[1 - \sqrt{1 - \frac{4}{3}\left(\frac{1}{1 + x}\right)^2} \right]^2. \tag{9}$$

Hence, both $h_{\text{inter}}/R_{\text{tot}}$ and ϕ_{inter} depend *only* on the overcrowding parameter x. The rest of the GNP volume (fraction) is occupied by the NP core and a dry layer of extended chains. For $R < R_{\text{tot}} - h_{\text{inter}}/2$, the thickness of the dry layer is given by

$$h_{\text{dry}} = R_{\text{tot}} - R - h_{\text{inter}}/2, \tag{10}$$

whereas no dry layer exists if $R > R_{\text{tot}} - h_{\text{inter}}/2$. In the latter case, our two-layer breaks down because the polymer corona is too thin to accommodate even unperturbed melt-like chains. Further, our theoretical model is physically meaningful only if there is enough polymer to uniformly fill the interstitial spaces between the NP cores. We can estimate this lower bound by considering the volume occupied by the grafted chains, $V_{\text{poly}} = ZN/\rho$, and the void space between closely packed bare NPs, $V_{\text{void}} = 8(\sqrt{8} - 2\pi/3)R^3$.[1] Therefore, we consider only cases where the conditions $R < R_{\text{tot}} - h_{\text{inter}}/2$ and $V_{\text{poly}}/V_{\text{void}} \quad 1$ are both satisfied.

Figure 2(a)-(d) shows a comparison of the theoretical predictions of h, h_{dry}, $h_{inter}/2$, and ϕ_{inter} with the corresponding simulation results (see Simulations section for details). We fixed the NP radius to $R = 7.5\sigma$ (σ being the diameter of a monomeric unit), and varied either the chain length N at fixed grafting density $\rho_g = 0.47\sigma^{-2}$ or varied ρ_g at fixed $N = 85$. For the theoretical calculations, we used the average monomer number density of our simulations $\rho = 0.9\sigma^{-3}$ (see Table 2) and the Kuhn length $b = 1.28\sigma$ of this polymer model. [52] Using instead the actual monomer number density measured in the simulations (see Table 2) leads to a change in brush thicknesses smaller than 2%, and was therefore disregarded for simplicity. For these parameters, our two-layer model is applicable for $N \gtrsim 7$ for GNPs with fixed $\rho_g = 0.47\sigma^{-2}$, and for $\rho_g \gtrsim 0.12\sigma^{-2}$ for GNPs with fixed $N = 85$. In all investigated cases, the theoretical predictions and simulation results for h, h_{dry} and $h_{inter}/2$ are in excellent agreement after we multiplied the theoretical curves by the shape factor $a \approx 0.93$ (see Fig. 2). For GNPs with fixed grafting density $\rho_g = 0.47\sigma^{-2}$, both h_{dry} and $h_{inter}/2$ increase with increasing N, with $h_{dry} > h_{inter}/2$ for the investigated range of N [see Fig. 2(a)]. For GNPs with fixed chain length $N = 85$, h_{dry} increases with increasing ρ_g while $h_{inter}/2$ decreases [see Fig. 2(b)]. The reduced thickness of the interpenetration layer, $h_{inter}/(2R_{tot})$, is a universal function monotonically decreasing with increasing x, with $h_{inter}/(2R_{tot}) \propto x^{-1}$ for large x (see ESI). Similarly, the normalized sum of dry layer thickness and NP radius, $(h_{dry} + R)/R_{tot}$, is a universal function monotonically increasing with increasing x [see Fig. 2(c)], with $(h_{dry} + R)/R_{tot} \propto 1 - x^{-1}$ for large x (see ESI). The volume fraction of the interpenetration layer, ϕ_{inter}, is a universal function of x which monotonically decreases with increasing x [see Fig. 2(d)], with $\phi_{inter} \propto 3x^{-1}$ for large x (see ESI). The excellent agreement of the theoretical curves with the simulation data confirms that the structure of GNPs of different grafting densities ρ_g and chain lengths N are identical if they have the same x.

Due to grafting and space-filling constraints, the densely grafted chains are extended in comparison to unperturbed polymers in a melt. To quantify this effect, we now consider the chain extension free energy

$$E_{ext} = \frac{3k_B T h^2}{2Nb^2} = \frac{3k_B T}{2Nb^2}\left[\left(R^3 + \frac{3ZN}{4\pi\rho}\right)^{1/3} - R\right]^2. \tag{11}$$

This chain extension energy is a function of the ratio $y = 3ZN/(4\pi\rho R^3)$ of the polymer shell volume ZN/ρ to the NP core volume $4\pi R^3/3$

$$E_{ext} = \frac{3k_B T}{8\pi}\frac{3Z}{\rho Rb^2}y^{-1}\left[(1 + y)^{1/3} - 1\right]^2 \tag{12}$$

where the coefficient $3Z/(Rb^2\rho)$ is the ratio of the polymer shell volume ZN/ρ to the volume of a cone with base area b^2N and height R. If the polymer shell volume is much smaller than the NP core volume, $y \ll 1$, then E_{ext} can be expanded with respect to y, leading to the planar brush result

$$E_{\text{ext}}^{\text{pln}} \approx \frac{k_{\text{B}}T}{8\pi} \frac{Zy}{\rho Rb^2} = \frac{3k_{\text{B}}T}{2} \left(\frac{Z}{4\pi \rho R^2 b} \right)^2 N. \tag{13}$$

In the opposite limit, $y \gg 1$, the chain extension energy decreases with increasing N because the layer thickness scales as $h \propto N^{1/3}$

$$E_{\text{ext}}^{\text{sph}} \approx \frac{9k_{\text{B}}T}{8\pi} \frac{Zy^{-1/3}}{\rho Rb^2} = \frac{3k_{\text{B}}T}{2} \left(\frac{3Z}{4\pi \rho b^3} \right)^{2/3} N^{-1/3}. \tag{14}$$

Thus, for small polymer to NP volume ratio $y \ll 1$, the chain extension free energy increases as $E_{\text{ext}} \propto y \propto N$, while for large volume ratio $y \gg 1$ it decreases as $E_{\text{ext}} \propto y^{-1/3} \propto N^{-1/3}$.

Therefore, E_{ext} goes through a maximum at $y_{\text{max}} = 6\sqrt{3} + 9 \approx 19.4$, corresponding to

$$N_{\text{max}} = 4\pi(2\sqrt{3} + 3)\frac{\rho R^3}{Z} \approx 81\frac{\rho R^3}{Z}. \tag{15}$$

This chain length corresponds to a polymer layer thickness

$$h_{\text{max}} = \left[(6\sqrt{3} + 10)^{1/3} - 1 \right] R = \sqrt{3} R \tag{16}$$

which is only $\sqrt{3}$ times larger than the NP radius. The value of the chain extension free energy at this maximum is

$$E_{\text{ext}}^{\text{max}} = \frac{3(2\sqrt{3} - 3)k_{\text{B}}T}{8\pi} \frac{Z}{\rho Rb^2} \approx 0.7k_{\text{B}}T\frac{\rho_{\text{g}}}{\rho b^2} R. \tag{17}$$

For the case of interest for our simulations, *i.e.*, $\rho_{\text{g}} = 0.47\sigma^{-2}$, $R = 7.5\sigma$, and $\rho = 0.9\sigma^{-3}$, the theoretically predicted maximum of E_{ext} is located at $N_{\text{max}} \approx 93$, as shown in Fig. 3(a). The simulation result for E_{ext} has a maximum at $N_{\text{max}} = 85$, which is in good agreement with the theoretical results when we multiply the latter by the square of the shape factor $\alpha^2 \approx 0.86$. The maximum of E_{ext} occurs at the same value of the volume ratio $y_{\text{max}} \approx 19.4$, independent on whether the chains are strongly extended ($E_{\text{ext}}^{\text{max}} \gg k_{\text{B}}T$) or not extended at all ($E_{\text{ext}}^{\text{max}} < k_{\text{B}}T$)), and is a result of the geometric crossover from a planar polymer layer around an NP (for small y) to a thick spherical polymer shell (for large y).

The case of interest for this work corresponds to GNPs which have a dry layer. It is interesting to note, that for such densely grafted NPs the spherical-like increase of the overall layer thickness $h \propto N^{1/3}$ can occur while chains are still strongly extended before GNPs enter the star polymer regime. This means that the geometric crossover of E_{ext} between the planar increase $E_{\text{ext}}^{\text{pln}} \propto N$ and spherical decrease $E_{\text{ext}}^{\text{sph}} \propto N^{-1/3}$ is predicted by the two-layer model with extended polymers over the wide range of parameter N on both

sides of the free energy maximum. Figure 3(a) demonstrates that the maximum of E_{ext} as a function of N and the decreasing chain extension free energy beyond this maximum are features that describe the GNPs of interest. In contrast, if the grafting density ρ_g (or Z) is varied at constant chain length N, then E_{ext} does not show a maximum but increases monotonically with increasing ρ_g (or Z) instead [see Fig. 3(b)].

Finally, we want to briefly discuss an alternative model for the theoretical description of GNPs. Kapnistos *et al.* proposed a scaling model to study the structure of multi-arm star polymers in a melt,[25] which can be adapted to our systems by including the contribution of the NP core. With this modification, the expression for the total brush thickness h becomes identical with our two-layer model given by Eq. (3), due to the incompressibility constraint and the conservation of the total volume. The two approaches differ, however, in the construction of the interpenetration layer. We assumed in our two-layer model that all grafted chains enter the interpenetration layer, whereas in the theory by Kapnistos *et al.* the number of chains in the interpenetration layer increases with decreasing overcrowding parameter x as $\tilde{Z} \propto Z x^{-1/3}$. Kapnistos *et al.* obtained the scaling of the interpenetration layer from the parabolic potential approximating the polymer layer by a planar brush, which leads to the scaling result $h_{inter} \propto b N^{1/2} x^{-1/6}$. We fitted this expression for h_{inter} to our simulation data (see Fig. 2), giving a prefactor of $\beta \approx 0.85$.

Despite these disparities, we observe that the predictions from both models for h, h_{dry}, and $h_{inter}/2$ are in good agreement with our simulation results for the investigated range of the overcrowding parameter $1.5 \lesssim x \lesssim 7$, see Fig. 2(a) and (b). The two models start to deviate for large x (see comparison between the two approaches in the ESI), for which the polymer corona becomes more planar ($h \ll R$). That regime is, however, outside of interest of this study. We emphasize that our simple analytical model for the GNPs provides an excellent description of h, h_{dry}, h_{inter}, and ϕ_{inter} across the range of interest to most experimental situations (see Figs. 2 and 3).

Simulations

We consider GNP melts for different values of the chain length N and grafting density ρ_g at fixed NP radius $R = 7.5\sigma$. The details of the simulations are provided in the Methods section. Figure 4 shows snapshots of single GNPs from these melts for various grafted chain lengths (a) $N = 15$, (b) $N = 85$ and (c) $N = 212$ at grafting density $\rho_g = 0.47\sigma^{-2}$, and for various grafting densities (d) $\rho_g = 0.15\sigma^{-2}$, (e) $\rho_g = 0.35\sigma^{-2}$ and (f) $\rho_g = 0.55\sigma^{-2}$ at chain length $N = 85$ for systems with random starting configurations. In this context we emphasize that, as discussed in the Methods section, the initial NP locations are at random, which should be contrasted with an ordered arrangement of initial NP locations on an FCC lattice, which is also considered in this work (see below). For fixed grafting density $\rho_g = 0.47\sigma^{-2}$, the overall size of the GNPs increases with increasing N, as expected. Similarly, for fixed chain length $N = 85$, the size of the GNPs increases with increasing ρ_g. Based on these snapshots, it appears that the spherical shape of the GNPs becomes increasingly distorted with the increase of N at fixed ρ_g, whereas the shape of the GNPs remains almost unaltered for fixed $N = 85$ and varying ρ_g (see Fig. 6 and accompanying discussion for a quantitative analysis of the shape of the GNPs).

The radial distribution functions of the NP centers, $g(r)$, are presented in Fig. 5 for three different grafted chain lengths $N = 15$, $N = 85$ and $N = 212$ at $\rho_g = 0.47\sigma^{-2}$, initialized from random NP locations. For all cases, we can see that $g(r)$ oscillates around one (black horizontal dashed line), indicating that the NPs have some local structure but are uniformly dispersed in the matrix of grafted polymers. The first peak of $g(r)$ at position r_{nn} represents the average separation between the nearest neighbor NPs, and r_{nn} shifts to larger distances as N is increased (see Table 1). Further, the first peak of $g(r)$ is relatively narrow for $N = 15$, but it becomes significantly broader for $N = 85$ and $N = 212$ at fixed ρ_g. Since the (normalized) peak width is characteristic of the rattling of the GNPs in a "cage", evidently the degree of GNP localization decreases with increasing chain length. This behavior can be rationalized by the increase of the volume fraction occupied by the interpenetration layer with increasing N, which leads to a softening of the effective interactions between the GNPs. A similar behavior is observed in the case of GNPs on an FCC lattice as well, but there the peaks are overall more pronounced due to the crystalline long-range order of the GNPs. The inset of Fig. 5 shows $g(r)$ for three different grafting densities, $\rho_g = 0.15\sigma^{-2}$, $\rho_g = 0.35\sigma^{-2}$ and $\rho_g = 0.55\sigma^{-2}$ at $N = 85$, for systems with random starting configurations. The nearest-neighbor distance r_{nn} increases with increasing ρ_g (see Table 1), but the (normalized) peak width is similar for all investigated ρ_g.

To quantify the size distribution of the GNPs, we have performed a Voronoi tessellation[54] around the centers of the NPs, and then computed the (normalized) distributions of the volume of the Voronoi cells, V_v. Figure 6(a) shows the distributions for selected N at fixed $\rho_g = 0.47\sigma^{-2}$ for both the random and ordered starting configurations. The width of the distributions increases with N, indicating that the correlation between NPs is becoming weaker with increasing N. This behavior is consistent with the prediction from our two-layer model that the volume fraction of the interpenetration layer, ϕ_{inter}, monotonically increases with increasing N at fixed ρ_g [see Fig. 2(d)]. The volume distributions in the systems initialized from an FCC lattice are much more narrow and show a weaker N-dependence compared to the random GNP configurations, reflecting the high symmetry of the FCC lattice. Irrespective of the starting configurations, the mean value of the distribution, $\langle V_v \rangle$, increases almost linearly with N. Similar behavior is observed for the GNP systems with varying ρ_g (or varying $Z = 4\pi R^2 \rho_g$) at fixed $N = 85$. This linear relationship $\langle V_v \rangle = (4/3)\pi R^3 + ZN/\rho = (4/3)\pi R_{tot}^3$ is expected, because the number of monomers per GNP (and thus the volume occupied by them) increases linearly with N at fixed ρ_g [see inset in Fig. 6(a)] or with ρ_g at fixed N.

The shape of the Voronoi cells and of the corona of the GNPs is probed *via* the asphericity parameter, S^2, defined as

$$S^2 = \frac{3}{2} \frac{\lambda_1^4 + \lambda_2^4 + \lambda_3^4}{\left(\lambda_1^2 + \lambda_2^2 + \lambda_3^2\right)^2} - \frac{1}{2}, \tag{18}$$

where λ_1, λ_2 and λ_3 are the eigenvalues of the gyration tensor (along the three principle axes) of the vertices of the Voronoi cell relative to the NP center, or of all of the monomers forming the corona of a GNP with respect to their center of mass. The value of S^2 is

bounded between zero and one. The lower limit $S^2 = 0$ is consistent with spherical symmetry ($\lambda_1 = \lambda_2 = \lambda_3$), while the upper limit $S^2 = 1$ indicates a rod-like shape. In Fig. 6(b) we present the average values of the asphericity parameter for the Voronoi cell $\left(S_v^2\right)$ and the polymer corona $\left(S_c^2\right)$ as functions of N at fixed $\rho_g = 0.47\sigma^{-2}$. Both S_v^2 and S_c^2 increase with N for the GNP systems with random NP starting configurations, indicating that the polymer coronas are becoming less spherical. In contrast, S_v^2 as well as S_c^2 increase much more slowly with N for the FCC starting configurations and have consistently smaller values compared to the random initial configurations. (Note that $S_v^2 = 0$ for a rhombic dodecahedron, which is the Voronoi cell of a perfect FCC lattice.) Nevertheless, the asphericity parameters remain rather low throughout, with the largest values of $S_v^2 \approx 0.15$ and $S_c^2 \approx 0.06$ for the GNPs with the longest grafts ($N = 212$) initialized from random GNP locations. For all GNP systems with varying ρ_g and fixed chain length $N = 85$, the values of S_v^2 and S_c^2 fluctuate around 0.05 and 0.13 (error is $< 5\%$), respectively. Thus, the polymer coronas are close to spherical supporting our initial assumption of the two-layer model.

The observed dependence of our results on the initial configurations is a strong indicator that the GNP systems have not reached global equilibrium in our simulations. There are two qualitatively different time scales that are evidently well separated from each other. The relaxation of the polymer brushes and the corresponding equilibration of the NPs within their nearest neighbor cages occurs at relatively short time scales, whereas the hopping of NPs between cages and the eventual diffusion of GNPs takes place on much longer time scales. Indeed, independent experimental rheology measurements of similar GNPs revealed that these cage rearrangements occur on macroscopic timescales (up to several days in some cases).[55] In our simulations, we have achieved the first stage of equilibration, *i.e.*, local relaxation of the grafted chains, but the entire system has not reached equilibrium.

To further analyze the distribution of the grafted polymers around the NPs, we computed radial monomer density profiles for the GNP systems with varying grafted chain lengths and grafting densities, as shown in Fig. 7(a)-(c). Here, we decompose the monomer density into two parts, $\rho = \rho_s + \rho_o$, where ρ_s is the contribution from polymers grafted to the same NP, while the contribution from other polymers is expressed in ρ_o. In all investigated cases, the total monomer density ρ fluctuates around the average monomer density in the system within our measurement uncertainty. For high grafting density $\rho_g = 0.47\sigma^{-2}$, we can see a distinct layering of monomers near the hard NP surface [see Fig. 7(a) and (b)], which decays within the range of a few monomers. However, no such layering is observed around the NP surface at the lowest grafting density $\rho_g = 0.15\sigma^{-2}$ [see Fig. 7(c)]. Further, in all cases ρ_s decays to zero at a distance $r \approx r_{nn} - 2R$, which indicates that the polymers fill the space between neighboring GNPs but do not wrap around them for the chosen set of simulation parameters. For $\rho_g = 0.47\sigma^{-2}$, ρ_o approaches zero as we move towards the NP surface, because the cores of the GNPs are completely surrounded by their own monomers. For $\rho_g = 0.15\sigma^{-2}$, the surrounding polymers from the other cores can easily interpenetrate, resulting in non-zero values of ρ_o even close to the NP surface [see Fig. 7(c)]. For comparison, the

radial density profiles for the FCC lattice starting configurations are presented in Fig. 7(a) and (b) as dashed lines, and we can see only minor deviations between the two cases.

To quantify the interpenetration of polymer coronas from neighboring GNPs, we computed the product of the radial monomer density profiles, $\rho_s\rho_o$, which is shown in Fig. 7(a)-(c) as orange lines. The full width at half maximum, δ, of the product of $\rho_s\rho_o$ provides a measure for the width of the interpenetration layer. We use the location of the maximum (corresponding to the distance where ρ_s and ρ_o cross) to extract the overall brush thickness, h_ρ. In Fig. 7(a) and (b), we have presented results from random and FCC lattice starting configurations. In both cases, the maxima of the distributions appear at similar locations, and thus provide similar values for the total brush thickness h_ρ, indicating that h_ρ does not depend on the starting configurations. Further, we identify the thickness of the dry layer by $h_{dry} = h_\rho - \delta/2$, and attribute the remaining part of the brush thickness to the interpenetration layer, *i.e.*, $h_{inter}/2 = h_\rho - h_{dry} = \delta/2$. Following this convention, the typical fraction of monomers from other GNPs in the dry layer is $5 - 6\%$ for all investigated cases (note that the two-layer model assumed strictly 0% and a sharp boundary between the dry and interpenetration layers). The resulting layer thicknesses are plotted in Fig. 2(a) and (b), which are in excellent agreement with the theoretical predictions. We also directly compute the average number of monomers (grafted to the same NP) in the dry layer, n_{dry}, and the average number of monomers $n_{inter} = N - n_{dry}$ in the interpenetration layer.

Next, we compare three different measures of the total brush thickness obtained from our simulations: (i) $h_v = [3\langle V_v\rangle/(4\pi)]^{1/3} - R$ is obtained by the Voronoi construction around the center of the NPs, assuming that the Voronoi cells are spherical (same definition as in our two-layer model); (ii) $h_{nn} = r_{nn}/2 - R$ has been extracted from the first peak of the radial distribution function between the NPs (see Fig. 5); (iii) h_ρ is the radially averaged location of the crossing of ρ_s and ρ_o, which corresponds to the center of the interpenetration layer formed by the polymer brushes of adjacent GNPs. The values for h_v, h_{nn}, and h_ρ are listed in Table 1 for all simulated systems, with $h_{nn} < h_\rho < h_v$. We used h_ρ to define the brush thickness in our simulations and all quantities derived from it. The differences between these values can be understood by considering the rhombic dodecahedral shape of the Voronoi cells in the simulations with FCC starting configurations (see Fig. 1(b) and ESI for details): The thickness h_{nn} corresponds to half of the face-to-face distance of the Voronoi cell, and for a perfect rhombic dodecahedron it is given by $h_{nn} = (\pi/\sqrt{18})^{1/3} R_{tot} - R \approx 0.9 R_{tot} - R < R_{tot} - R = h_v$. If the crossing of ρ_s and ρ_o occurs exactly on the surface of the rhombic dodecahedron, then geometric considerations lead to $h\rho \approx 1.115 (\pi/\sqrt{18})^{1/3} R_{tot} - R > h_v$. We found, however, that these crossings occur at slightly shorter distances compared to the surface of a perfect rhombic dodecahedron, so that the measured h_ρ is somewhat smaller than theoretically expected. To account for this discrepancy, we introduce an empirical shape factor $a \approx 0.93$ based on our simulation results, and multiply all theoretical expressions for the brush thickness (*i.e.*, h, h_{dry}, and $h_{inter}/2$) by this factor.

Figure 8(a) shows the values of the fraction of monomers in the interpenetration zone n_{inter}/N as functions of N at fixed $\rho_g = 0.47\sigma^{-2}$. The results from theory and simulation are in good agreement with each other, exhibiting the same trends: for small N, the ratio n_{inter}/N decreases with N due to the faster growth of the dry layer in this regime, while n_{inter}/N

gradually increases with N for large N, resulting in a minimum at intermediate N. Note that $\phi_{inter}(N)$ decays monotonically with increasing N for the same parameters [*cf.* Fig. 2(d)], as the calculation of ϕ_{inter} includes the NP core in the denominator as discussed in the Two-Layer Model section. The values of n_{inter}/N for the GNP systems with varying ρ_g at fixed $N = 85$ are plotted in Fig. 8(b). In this case, both the theory and the simulations show that n_{inter}/N gradually decreases with increasing grafting density ρ_g for fixed N.

To better understand the conformational details of the grafted chains, we computed the polymer end-to-end vector $\mathbf{R}_e$ and its radial ($R_{e,r}$) and transverse ($R_{e,t}$) components, both for the entire chains and for chain segments of length n. We first determined from our simulation data the probability distribution functions of the squared end-to-end distances of the entire grafted chains, $P\left(\left\langle R_e^2 \right\rangle\right)$, revealing that the grafted chains are always more extended than polymers of the same length in a pure melt (see Fig. S5 in ESI). Chain sections close to the NP surface have different conformations compared to chain sections at the periphery of the polymer corona because of steric crowding effects. To quantify the local polymer conformation, we have computed $\left\langle R_{e,r} \right\rangle$ for subsections of fixed length $n = 20$ along the chain contour. Figure 9 shows $\left\langle R_{e,r} \right\rangle^2$ of these chain sections (the average transverse components $\left\langle R_{e,t} \right\rangle$ are always zero within statistical fluctuations), normalized by the mean-square end-to-end distance in a pure polymer melt $\left\langle R_{e,0}^2(n) \right\rangle/3$. All results are shown as functions of the chain section origin n_{ori} ($n_{ori} = 0$ corresponds to the grafting point) for GNP systems with (a) varying N at $\rho_g = 0.47\sigma^{-2}$ and (b) varying ρ_g at $N = 85$. In our two-layer model, $3\left\langle R_{e,r} \right\rangle^2/\left\langle R_{e,0}^2 \right\rangle = 3[h(n_{ori} + n) - h(n_{ori})]^2/\left(nb^2\right)$, which is also included in Fig. 9. In Fig. S6 of the ESI, we have plotted $3\left\langle R_{e,r} \right\rangle^2/\left\langle R_{e,0}^2 \right\rangle$ as functions of number n of monomers in chain section, while fixing one chain end at the grafting point ($n_{ori} = 0$).

In both theory and simulations, there is a pronounced extension of chain sections near the NP surface in all cases, followed by a monotonic decrease of $3\left\langle R_{e,r} \right\rangle^2/\left\langle R_{e,0}^2 \right\rangle$ with increasing n_{ori}. For a given n_{ori}, $3\left\langle R_{e,r} \right\rangle^2/\left\langle R_{e,0}^2 \right\rangle$ increases with increasing grafting density ρ_g in both the dry and interpenetration layer of the polymer corona. In our simulations, chain sections deep in the interpenetration layer approach $\left\langle R_{e,r} \right\rangle^2 \approx 0$, whereas $\left\langle R_{e,r} \right\rangle^2 > 0$ in our two-layer model for all n_{ori}. Further, the theoretical extension of chain sections was independent of the total chain length N, which is a consequence of our approximation that all grafted chains behave in the same way and uniformly fill the volume between $h(n_{ori})$ and $h(n_{ori} + n)$. We have also computed the fluctuations of the radial and transverse components of $\mathbf{R}_e(n)$ of these chain sections relative to fluctuations in pure polymer melts, $3\left(\left\langle R_{e,r}^2 \right\rangle - \left\langle R_{e,r} \right\rangle^2\right)/\left\langle R_{e,0}^2 \right\rangle$ and $3\left(\left\langle R_{e,t}^2 \right\rangle - \left\langle R_{e,t} \right\rangle^2\right)/\left(2\left\langle R_{e,0}^2 \right\rangle\right)$, respectively. These data are shown in the inset of Fig. 9 as functions of n_{ori} for fixed $n = 20$, demonstrating that the fluctuations along the radial direction are strongly suppressed in all cases. In contrast, transverse fluctuations were slightly enhanced for N 85 but suppressed for $N > 85$. Figures S6(a) and S6(b) in the ESI show the square of the normalized average radial size as functions of n at fixed $n_{ori} = 0$, while the relative fluctuations are plotted in Figs. S6(c) and S6(d).

Conclusions

In this work we studied the structure of polymer-grafted nanoparticles (GNPs) *via* coarse-grained molecular dynamics simulations by systematically varying the degree of polymerization of the grafted polymers and their grafting density at fixed NP radius. The total brush thickness of the GNPs, h, was decomposed into two separate layers: a *dry layer* of extended chains, where only few monomers from the surrounding GNPs were present, and an *interpenetration layer* of unperturbed chains, where significant overlap between grafted chains of the surrounding GNPs occurred, presumably to maximize their conformational entropy. The thicknesses of the dry layer, h_{dry}, and of the interpenetration layer, h_{inter}, were estimated by a simple spherical two-layer model. According to our theory, the behavior of h, h_{dry} and h_{inter} can be described by a single universal parameter, x, which compares the actual number of graft chains on an NP, Z, to what is expected for the number of overlapping unperturbed chains in a melt with the same volume as the GNP (with both the core and corona included). This crowding parameter x decreases with increasing graft length N at fixed grafting density ρ_g, whereas x increases with increasing ρ_g at fixed N. Thus, $x \approx 1$ for unperturbed chains (*e.g.* sparsely grafted NPs with long grafts), while $x \gg 1$ for strongly extended chains (*e.g.* densely grafted NPs with short grafts). We find that this two-layer model works well in the range of our simulations $1 \lesssim x \lesssim 7$.

For GNPs with fixed grafting density ρ_g, both h_{dry} and $h_{inter}/2$ increase with increasing N, with $h_{dry} > h_{inter}/2$ for the investigated range of N at $\rho_g = 0.47\sigma^{-2}$. When the chain length N is fixed and ρ_g is varied instead, h_{dry} increases with increasing ρ_g whereas $h_{inter}/2$ decreases. For sufficiently small ρ_g, h_{dry} is smaller than $h_{inter}/2$, but these two curves cross at some intermediate ρ_g so that eventually $h_{inter}/2 > h_{dry}$ at large enough ρ_g. We also predict that the volume fraction of the interpenetration layer, ϕ_{inter}, is a universal function of x which decays monotonically with increasing x. All these predictions from our two-layer scaling model are in quantitative agreement with simulation results after we account for the slightly distorted shape of the polymer coronas. Most importantly, we predict a peak of the chain extension energy $3k_B T h^2/(2Nb^2)$ at $N_{max} \approx 81(\rho R^3)/Z$, which for our system with $\rho_g = 0.47\sigma^{-2}$, $R = 7.5\sigma$, $\rho = 0.9\sigma^{-3}$ is $N_{max} \approx 93$. For grafts with $N = N_{max}$, the total brush thickness is $h = \sqrt{3} R$, independent of grafting density ρ_g and monomer density ρ. The associated maximum value of the extension energy is $E_{ext} \approx 0.055 a^2 k_B T Z/(\rho R b^2)$, which is $\approx 1.4 k_B T$ for our case ($Z = 332$, $a \approx 0.93$).

Our theoretical model is useful for designing pure melts of GNPs with tailored structural properties, for instance optimizing the degree of polymer interpenetration at a given NP volume fraction. Further, the theoretical knowledge gained from this work provides a starting point for investigating systems to which an additional free component, such as small molecules or ungrafted polymers, are added. For example, it is conceivable that small additives become homogeneously dispersed in the polymer brush, whereas large additives could occupy the interstitial sites between the polymer coronas. A conjecture could be that the optimal condition for this partitioning to occur is at the maximum chain extension energy. It will also be interesting to investigate the structural properties of anisotropic GNPs with high aspect ratios.

Methods

The grafted polymers are represented by a bead-spring model, where a chain consists of N spherical beads, each with diameter σ and mass m. The bonds between the individual monomers are modeled *via* the finitely extensible nonlinear elastic (FENE) potential[56,57]

$$U_{\text{FENE}}(r) = -\frac{k}{2}r_0^2\ln\left[1 - \left(\frac{r}{r_0}\right)^2\right].$$

(19)

Here, r_0 is the maximum bond length and k is the spring constant. To prevent unphysical bond crossing, which will impact our associated study on system dynamics, we employed the standard Kremer-Grest parameterization,[56,57] *i.e.*, $r_0 = 1.5\sigma$ and $k = 30\varepsilon/\sigma^2$.

The interaction between any two monomers separated by distance r is represented by the standard Lennard-Jones (LJ) potential

$$U_{\text{MM}}(r) = \begin{cases} 4\varepsilon\left[\left(\dfrac{\sigma}{r}\right)^{12} - \left(\dfrac{\sigma}{r}\right)^{6}\right] & \text{for } r \leq r_{\text{c}} \\ 0 & \text{for } r > r_{\text{c}}, \end{cases}$$

(20)

with cut-off distance $r_{\text{c}} = 3\sigma$, and interaction strength $\varepsilon = k_{\text{B}}T$. The pair potential $U_{\text{MM}}(r)$ is multiplied with a smoothing polynomial, $S(r)$, for distances r $r_{\text{sm}} = 2.5\sigma$, to gradually decrease both the potential and force to zero at $r = r_{\text{c}}$. The functional form of $S(r)$ is

$$S(r) = \frac{\left(r_{\text{c}}^2 - r^2\right)^2\left(r_{\text{c}}^2 + 2r^2 - 3r_{\text{sm}}^2\right)}{\left(r_{\text{c}}^2 - r_{\text{sm}}^2\right)^3}.$$

(21)

The hard NPs are modeled as smooth spherical spheres with radius R. The NP-NP interaction is described by the shifted Lennard-Jones (sLJ) potential

$$U_{\text{NN}}(r) = \begin{cases} 4\varepsilon\left[\left(\dfrac{2R}{r - \Delta}\right)^{12} - \left(\dfrac{2R}{r - \Delta}\right)^{6}\right] & \text{for } r \leq r_{\text{sLJ}} + \Delta \\ 0 & \text{for } r > r_{\text{SLJ}} + \Delta, \end{cases}$$

(22)

with $= 2R - 1$ and cut-off distance $r_{\text{SLJ}} = 2^{1/6}\sigma$ to make U_{NN} purely repulsive. The interaction between a monomer and an NP is also described by the sLJ potential with $=$ $(2R + \sigma)/2 - 1$ in Eq. (22).

The polymers are grafted to the NPs by rigidly attaching the first polymer bead to the NP surface. These immobile grafting points are randomly distributed on the NP surface with a minimum distance of σ. Then, the remainder of the chains are connected to those grafting beads using the FENE potential (see the schematic representation given in Fig. 10).

Throughout all our simulations, we set the radius of the NPs to $R = 7.5\sigma$ and either varied the degree of polymerization N at fixed grafting density $\rho_{\text{g}} = 0.47\sigma^{-2}$, or varied ρ_{g} at fixed N = 85 (a summary of the simulated systems is given in Table 2). Note that for $\sigma = 1$nm, this

model matches the experimental systems studied by Bilchak *et al.*[51] All our MD simulations are performed using the HOOMD-blue software package (v. 2.5.1) with double-precision floating-point operations.[58–60] Periodic boundary conditions are applied along the x, y and z directions. We set the simulation time step to $t = 0.002\,\tau$, where $\tau = \sqrt{m\sigma^2/(k_\mathrm{B}T)}$ is the intrinsic MD unit of time.

In order to study the effect of the NP arrangement, we generated starting configurations where the GNPs are either randomly placed in the simulation box or on an FCC lattice. Initially, N_NP GNPs are distributed in a cubic box, with its edge length chosen such that the polymer coronas of the GNPs do not overlap. Next, an isotropic compression is applied, until we reach a monomer density (typically between $0.7\sigma^{-3}$ and $0.8\sigma^{-3}$) close to the one at equilibrium, $\rho \approx 0.9\sigma^{-3}$. During this process, all interactions are set to purely repulsive. In the next step, we turn on the attractive contributions of the pair potentials, and simulate over 2×10^7 time steps in the $\mathcal{N}PT$ ensemble at fixed pressure $P = 0\varepsilon/\sigma^3$ and temperature $T = \varepsilon/k_\mathrm{B}$. After equilibrating the system in the $\mathcal{N}PT$ ensemble, we compute the time-averaged volume of the system, and simulate for 10^7 time steps at this volume in the $\mathcal{N}VT$ ensemble, using a Langevin thermostat. For the final production runs, we perform simulations in the $\mathcal{N}VE$ ensemble for at least 5×10^7 time steps. The volume fraction of NPs in the system is then $\phi_\mathrm{NP} = 4\pi R^3 N_\mathrm{NP}/(3\,V)$. All results presented for the GNP systems with random starting configurations are averaged over three independent initializations, while we use a single starting configuration for the systems initialized on an FCC lattice. We found that the final box volume, and thus also the monomer density ρ and NP loading ϕ_NP, did not depend on the starting configuration.

Supplementary Material

Refer to Web version on PubMed Central for supplementary material.

Acknowledgments

References

1. Allen TM; Cullis PR Drug Delivery Systems: Entering the Mainstream. Science 2004, 303, 1818–1822. [PubMed: 15031496]

2. De M; Ghosh PS; Rotello VM 'Applications of Nanoparticles in Biology'. Adv. Mater 2008, 22, 4225–4241.

3. Sun T; Zhang YS; Pang B; Hyun DC; Yang M; Xia Y. Engineered Nanoparticles for Drug Delivery in Cancer Therapy. Angew. Chem. Int 2014, 53, 12320–12364.

4. Galizia M; Chi WS; Smith ZP; Merkel TC; Baker RW; Freeman BD 50th Anniversary Perspective: Polymers and Mixed Matrix Membranes for Gas and Vapor Separation: A Review and Prospective Opportunities. Macromolecules 2017, 50, 7809–7843.

5. Pandey N; Shukla SK; Singh NB Water Purification by Polymer Nanocomposites: An Overview. Nanocomposites 2017, 3, 47–66.

6. Barnett JW; Kumar SK Modeling Gas Transport in Polymer-Grafted Nanoparticle Membranes. Soft Matter 2019, 15, 424–432. [PubMed: 30569058]

7. Hosein ID; Lee SH; Liddell CM Dimer-Based Three-Dimensional Photonic Crystals. Adv. Funct. Mater 2010, 20, 3085–3091.

8. Ding T; Song K; Clays K; Tung C-H Fabrication of 3D Photonic Crystals of Ellipsoids: Convective Self-Assembly in Magnetic Field. Adv. Mater 2009, 21, 1936–1940.

9. Beltramo PJ; Schneider D; Fytas G; Furst EM Anisotropic Hypersonic Phonon Propagation in Films of Aligned Ellipsoids. Phys. Rev. Lett 2014, 113, 205503. [PubMed: 25432048]

10. Kim H; Cang Y; Kang E; Graczykowski B; Secchi M; Montagna M; Priestley RD; Furst EM; Fytas G. Direct Observation of Polymer Surface Mobility via Nanoparticle Vibrations. Nat. Commun 2018, 9, 2041–1723. [PubMed: 29795268]

11. Green DL; Mewis J. Connecting the Wetting and Rheological Behaviors of Poly(dimethylsiloxane)-Grafted Silica Spheres in Poly(dimethylsiloxane) Melts. Langmuir 2006, 22, 9546–9553. [PubMed: 17073478]

12. Akcora P; Liu H; Kumar SK; Moll J; Li Y; Benicewicz BC; Schadler LS; Acehan D; Panagiotopoulos AZ; Pryamitsyn V et al. Anisotropic Self-Assembly of Spherical Polymer-Grafted Nanoparticles. Nat. Mater 2009, 8, 354–359. [PubMed: 19305399]

13. Agarwal P; Qi H; Archer LA The Ages in a Self-Suspended Nanoparticle Liquid. Nano Lett. 2010, 10, 111–115. [PubMed: 19950934]

14. Kim D; Archer LA Nanoscale OrganicInorganic Hybrid Lubricants. Langmuir 2011, 27, 3083–3094. [PubMed: 21280594]

15. Kumar SK; Jouault N; Benicewicz B; Neely T. Nanocomposites with Polymer Grafted Nanoparticles. Macromolecules 2013, 46, 3199–3214.

16. Chandran S; Saw S; Kandar AK; Dasgupta C; Sprung M; Basu JK Suspensions of Polymer-Grafted Nanoparticles with Added PolymersStructure and Effective Pair-Interactions. J. Chem. Phys 2015, 143, 084902.

17. Choudhury S; Agrawal A; Kim SA; Archer LA Self-Suspended Suspensions of Covalently Grafted Hairy Nanoparticles. Langmuir 2015, 31, 3222–3231. [PubMed: 25712578]

18. Cheng S; Carroll B; Bocharova V; Carrillo J-M; Sumpter BG; Sokolov AP Focus: Structure and Dynamics of the Interfacial Layer in Polymer Nanocomposites with Attractive Interactions. J. Chem. Phys 2017, 146, 203201. [PubMed: 28571333]

19. Lenart WR; Hore MJ StructureProperty Relationships of Polymer-Grafted Nanospheres for Designing Advanced Nanocomposites. Nano-Struct. Nano-Objects 2018, 16, 428–440.

20. Daoud M; Cotton JP Star shaped polymers: A model for the conformationand its concentration dependence. J. Physique 1982, 43, 531–538.

21. Ohno K; Morinaga T; Takeno S; Tsuji Y; Fukuda T. Suspensions of Silica Particles Grafted with Concentrated Polymer Brush: Effects of Graft Chain Length on Brush Layer Thickness and Colloidal Crystallization. Macromolecules 2007, 40, 9143–3150.

22. Zhulina EB Phase diagram for semi-rigid macromolecules grafted to a solid sphere. Polymer Science U.S.S.R. 1984, 26, 885–891.

23. Birshtein TM; Zhulina EB Conformations of star-branched macromolecules. Polymer 1984, 25, 1453–1461.

24. Birshtein TM; Zhulina EB; Borisov OV Temperature-concentration diagram for a solution of star-branched macromolecules. Polymer 1986, 27, 1078–1086.

25. Kapnistos M; Semenov AN; Vlassopoulos D; Roovers J. Viscoelastic Response of Hyperstar Polymers in the Linear Regime. J. Chem. Phys 1999, 111, 1753–1759.

26. Rafiee MA; Rafiee J; Wang Z; Song H; Yu Z-Z; Koratkar N. Enhanced Mechanical Properties of Nanocomposites at Low Graphene Content. ACS Nano 2009, 3, 3884–3890. [PubMed: 19957928]

27. Cheng S; Bocharova V; Belianinov A; Xiong S; Kisliuk A; Somnath S; Holt AP; Ovchinnikova OS; Jesse S; Martin H et al. Unraveling the Mechanism of Nanoscale Mechanical Reinforcement in Glassy Polymer Nanocomposites. Nano Lett. 2016, 16, 3630–3637. [PubMed: 27203453]

28. Ethier JG; Hall LM Structure and Entanglement Network of Model Polymer-Grafted Nanoparticle Monolayers. Macromolecules 2018, 51, 9878–9889.

29. Ji T; Ma C; Brisbin L; Dong Y; Zhu J. Effect of Interface on the Mechanical Behavior of PolybutadieneSilica Composites: An Experimental and Simulation Study. J. Appl. Polym. Sci 2018, 135, 46089.

30. Midya J; Cang Y; Egorov SA; Matyjaszewski K; Bockstaller MR; Nikoubashman A; Fytas G. Disentangling the Role of Chain Conformation on the Mechanics of Polymer Tethered Particle Materials. Nano Lett. 2019, 19, 2715–2722. [PubMed: 30913883]

31. Hansoge NK; Huang T; Sinko R; Xia W; Chen W; Keten S. Materials by Design for Stiff and Tough Hairy Nanoparticle Assemblies. ACS Nano 2018, 12, 7946–7958. [PubMed: 29975847]

32. Yang S; Akcora P. Deformation of Chemically Heterogeneous Interfacial Layers of Polymer Nanocomposites. ACS Macro Lett. 2019, 8, 1635–1641.

33. Bilchak CR; Huang Y; Benicewicz BC; Durning CJ; Kumar SK High-Frequency Mechanical Behavior of Pure Polymer-Grafted Nanoparticle Constructs. ACS Macro Lett. 2019, 8, 294–298.

34. Li Y; Tao P; Viswanath A; Benicewicz BC; Schadler LS Bimodal Surface Ligand Engineering: The Key to Tunable Nanocomposites. Langmuir 2013, 29, 1211–1220. [PubMed: 23092225]

35. Wang Z; Lu Z; Mahoney C; Yan J; Ferebee R; Luo D; Matyjaszewski K; Bockstaller MR Transparent and High Refractive Index Thermoplastic Polymer Glasses Using Evaporative Ligand Exchange of Hybrid Particle Fillers. ACS Appl. Mater. Interfaces 2017, 9, 7515–7522. [PubMed: 28171720]

36. McGrail BT; Sehirlioglu A; Pentzer E. Polymer Composites for Thermoelectric Applications. Angew. Chem. Int 2015, 54, 1710–1723.

37. Sunday DF; Green DL Thermal and Rheological Behavior of Polymer Grafted Nanoparticles. Macromolecules 2015, 48, 8651–8659.

38. Grabowski CA; Koerner H; Meth JS; Dang A; Hui CM; Matyjaszewski K; Bockstaller MR; Durstock MF; Vaia RA Performance of Dielectric Nanocomposites: Matrix-Free, Hairy Nanoparticle Assemblies and Amorphous PolymerNanoparticle Blends. ACS Appl. Mater. Interfaces 2014, 6, 21500–21509. [PubMed: 25365781]

39. Kim SA; Mangal R; Archer LA Relaxation Dynamics of Nanoparticle-Tethered Polymer Chains. Macromolecules 2015, 48, 6280–6293.

40. Wood AB A Textbook of Sound; Being an Account of the Physics of Vibrations with Special Reference to Recent Theoretical and Technical Developments, 2nd ed.; New York, The Macmillan company, 1941.

41. Kumar SK; Krishnamoorti R. Nanocomposites: Structure, Phase Behavior, and Properties. Annu. Rev. Chem. Biomol. Eng 2010, 1, 37–58. [PubMed: 22432572]

42. Chremos A; Panagiotopoulos AZ Structural Transitions of Solvent-Free Oligomer-Grafted Nanoparticles. Phys. Rev. Lett 2011, 107, 105503. [PubMed: 21981510]

43. Ganesan V; Jayaraman A. Theory and Simulation Studies of Effective Interactions, Phase Behavior and Morphology in Polymer Nanocomposites. Soft Matter 2014, 10, 13–38. [PubMed: 24651842]

44. Chremos A; Douglas JF Self-Assembly of Polymer-Grafted Nanoparticles in Solvent-Free Conditions. Soft Matter 2016, 12, 9527–9537. [PubMed: 27841418]

45. Yatsyshin P; Fytas NG; Theodorakis PE MixingDemixing Transition in Polymer-Grafted Spherical Nanoparticles. Soft Matter 2020, 16, 703–708. [PubMed: 31819935]

46. Koski JP; Krook NM; Ford J; Yahata Y; Ohno K; Murray CB; Frischknecht AL; Composto RJ; Riggleman RA Phase Behavior of Grafted Polymer Nanocomposites from Field-Based Simulations. Macromolecules 2019, 52, 5110–5121.

47. Hou G; Xia X; Liu J; Wang W; Dong M; Zhang L. Designing Superlattice Structure via Self-Assembly of One-Component Polymer-Grafted Nanoparticles. J. Phys. Chem. B 2019, 123, 2157–2168. [PubMed: 30742436]

48. Lafitte T; Kumar SK; Panagiotopoulos AZ Self-Assembly of Polymer-Grafted Nanoparticles in Thin Films. Soft Matter 2014, 10, 786–794. [PubMed: 24834986]

49. Ma S; Hu Y; Wang R. Amphiphilic Block Copolymer Aided Design of Hybrid Assemblies of Nanoparticles: Nanowire, Nanoring, and Nanocluster. Macromolecules 2016, 49, 3535–3541.

50. Beltran-Villegas DJ; Jayaraman A. Assembly of Amphiphilic Block Copolymers and Nanoparticles in Solution: Coarse-Grained Molecular Simulation Study. J. Chem. Eng. Data 2018, 63, 2351–2367.

51. Bilchak CR; Buenning E; Asai M; Zhang K; Durning CJ; Kumar SK;Huang Y; Benicewicz BC; Gidley DW; Cheng S et al. Polymer-Grafted Nanoparticle Membranes with Controllable Free Volume. Macromolecules 2017, 50, 7111–7120.

52. Chremos A; Nikoubashman A; Panagiotopoulos AZ Flory-Huggins Parameter χ, From Binary Mixtures of Lennard-Jones Particles to Block Copolymer Melts. J. Chem. Phys 2014, 140, 054909.

53. Humphrey W; Dalke A; Schulten K. VMD - Visual Molecular Dynamics. J. Molec. Graphics 1996, 14, 33–38.

54. Ramasubramani V; Dice BD; Harper ES; Spellings MP; Anderson JA; Glotzer SC freud: A Software Suite for High Throughput Analysis of Particle Simulation Data. Comput. Phys. Commun 2020, 254, 107275.

55. Parisi D; Buening E; Gury L; Benicewicz BC; Cloitre M; Rubinstein M; Kumar SK; Vlassopoulos D Jammed Colloidal Dynamics in Self-Suspended Grafted Nanoparticle Melts. (unpublished).

56. Kremer K; Grest GS Dynamics of Entangled Linear Polymer Melts: A Molecular-Dynamics Simulation. J. Chem. Phys 1990, 92, 5057–5086.

57. Grest GS; Kremer K. Molecular Dynamics Simulation for Polymers in the Presence of a Heat Bath. Phys. Rev. A 1986, 33, 3628–3631.

58. Anderson JA; Lorenz CD; Travesset A. General Purpose Molecular Dynamics Simulations Fully Implemented on Graphics Processing Units. J. Comput. Phys 2008, 227, 5342–5359.

59. Glaser J; Nguyen TD; Anderson JA; Lui P; Spiga F; Millan JA; Morse DC; Glotzer SC Strong Scaling of General-Purpose Molecular Dynamics Simulations on GPUs. Comput. Phys. Commun 2015, 192, 97–107.

60. Howard MP; Anderson JA; Nikoubashman A; Glotzer SC; Panagiotopoulos AZ Efficient Neighbor List Calculation for Molecular Simulation of Colloidal Systems Using Graphics Processing Units. Comput. Phys. Commun 2016, 203, 45–52.
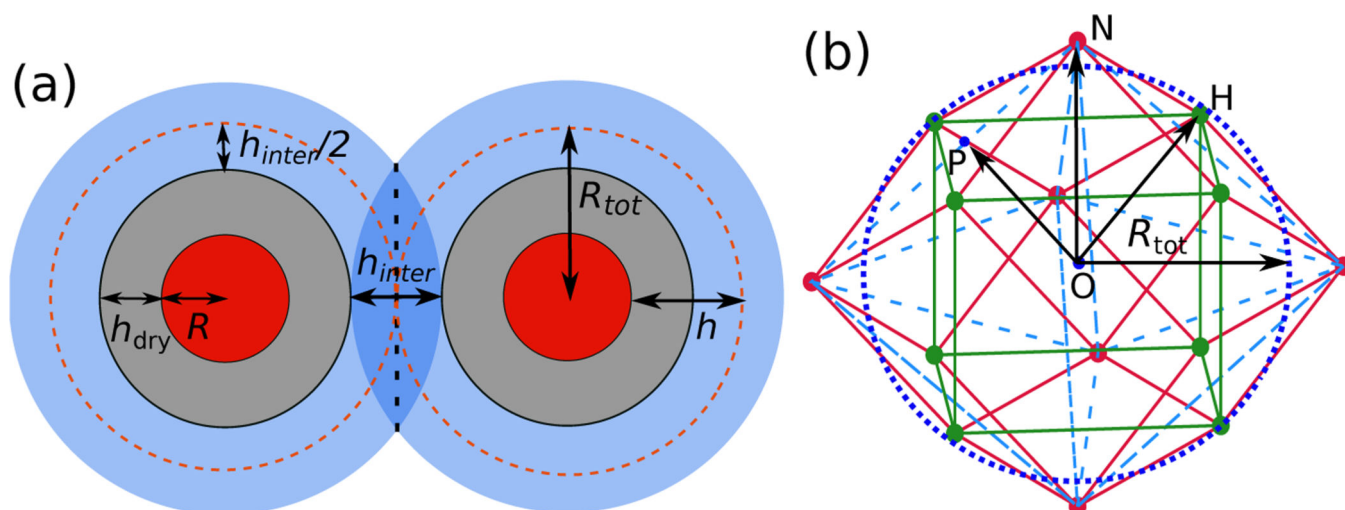
Figure 1:
(a) Schematic representation of the two-layer model, indicating the NP radius, R, the total radius of the GNP, R_{tot}, and the thicknesses of the dry and interpenetration layers, h_{dry} and h_{inter}, respectively. (b) Voronoi cell (rhombic dodecahedron) for the face-centered cubic (FCC) packing of spheres. The center of the cell is indicated by O and the mid point of one of the rhombic faces is indicated by P. The vector from O to P points to the nearest neighbor, and its length is given by the lattice constant of the FCC crystal, $|\mathbf{OP}| = a_0$. The vector from O to H points to the next-nearest neighbor and has a length of $|\mathbf{OH}| = \sqrt{3/2}a_0$, while the vector pointing from O to N has a length of $|\mathbf{ON}| = \sqrt{2}a_0$. The sphere (blue dashed line) with radius R_{tot} has the same volume as the Voronoi cell.
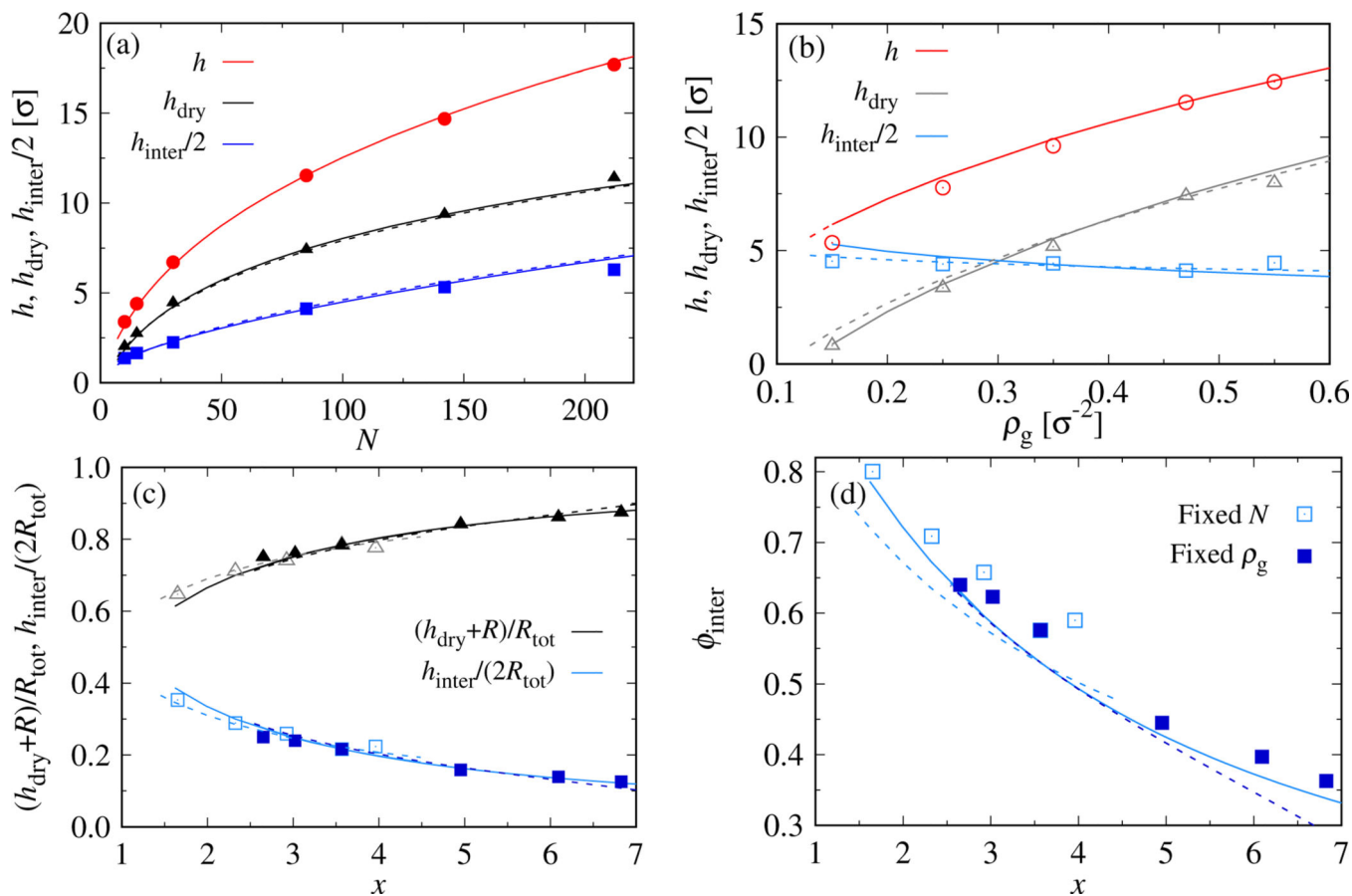
Figure 2:

(a, b) Total brush thicknesses $h = h_{dry} + h_{inter}/2$, thickness of the dry layer h_{dry}, and half thickness of the interpenetration layer $h_{inter}/2$ plotted (a) as a function of chain length N at fixed grafting density $\rho_g = 0.47\sigma^{-2}$, and (b) as a function of ρ_g at fixed $N = 85$. In both cases $R = 7.5\sigma$ fixed. (c) Reduced thicknesses $h_{inter}/(2R_{tot})$ and $(h_{dry} + R)/R_{tot}$ as functions of x. $[(h_{dry} + R)/R_{tot} + h_{inter}/(2R_{tot}) = 1.]$ Filled and open symbols correspond to the data shown in panels (a) and (b), respectively. (d) Volume fraction of the interpenetration layer, ϕ_{inter}, as a function of x for systems shown in (a, b). In all panels, symbols show our simulation results (initialized from random NP locations), while solid lines are theoretical predictions from our two-layer model. The dashed lines are the theoretical predictions of the modified model of Kapnistos *et al.*[25]
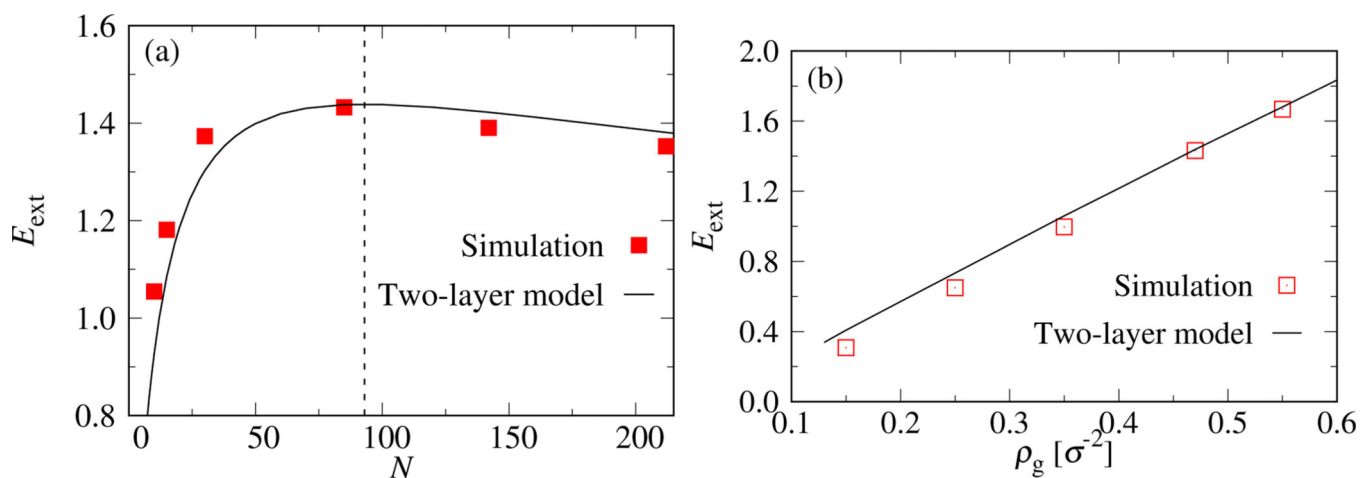
Figure 3:
Chain extension free energy, E_{ext}, as a function of (a) N for fixed $\rho_g = 0.47\sigma^{-2}$ and (b) ρ_g for fixed $N = 85$. Symbols are simulation results (initialized from random NP locations), and the black solid lines indicate the theoretical predictions from the two-layer model and the modified model of Kapnistos *et al.*[25] The vertical dashed line in (a) indicates the position of the maximum of the theoretical curve.
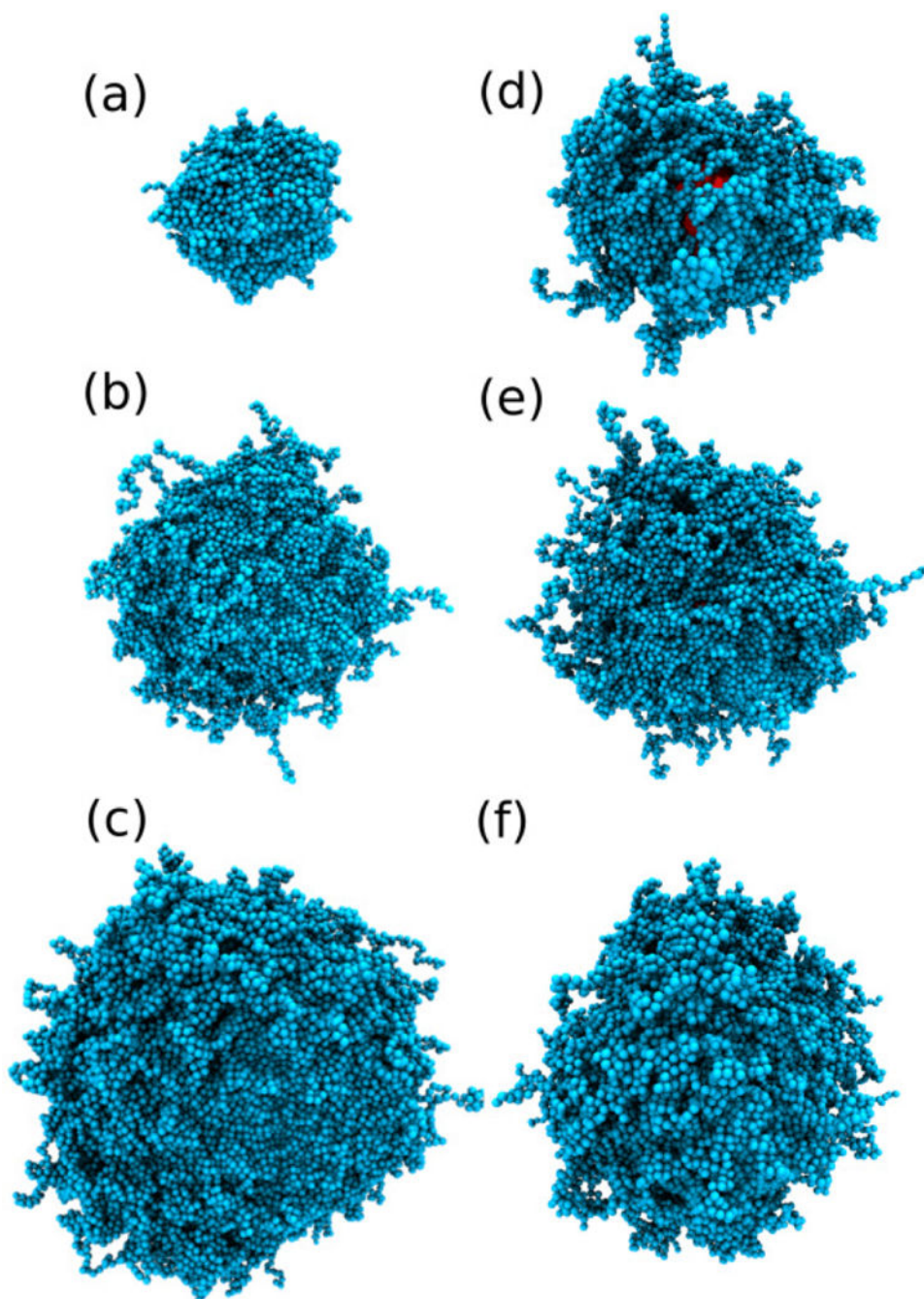
Figure 4:
Simulation snapshots of a single GNP in a bulk system with varying chain lengths, (a) $N = 15$, (b) $N = 85$ and (c) $N = 212$ at $\rho_g = 0.47\sigma^{-2}$, and with varying grafting densities, (d) $\rho_g = 0.15\sigma^{-2}$, (e) $\rho_g = 0.35\sigma^{-2}$ and (f) $\rho_g = 0.55\sigma^{-2}$ at $N = 85$. Snapshots have been taken from the systems initialized from random starting configurations, and they have been rendered using Visual Molecular Dynamics v 1.9.3.[53]
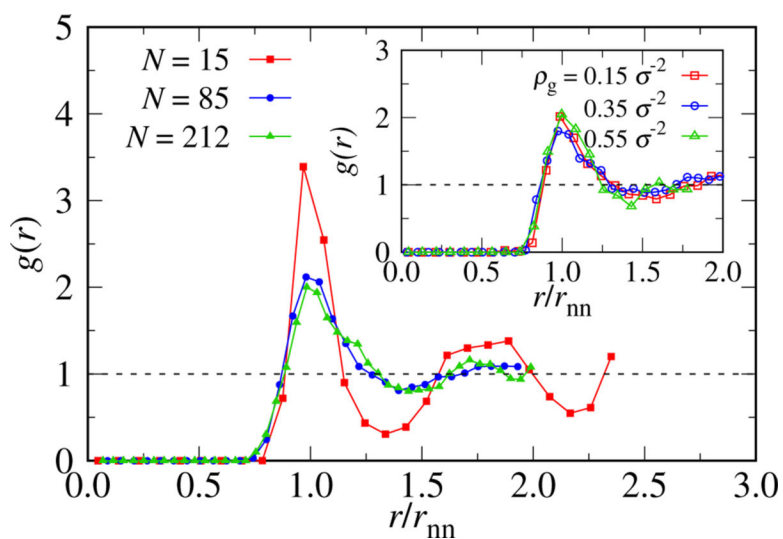
Figure 5:
Radial distribution function, $g(r)$, between centers of NPs with random starting configurations. The inset shows $g(r)$ for GNP systems with different grafting densities at fixed chain length $N = 85$. In both plots, the x-axis is scaled with the average nearest-neighbor distance, r_{nn}.
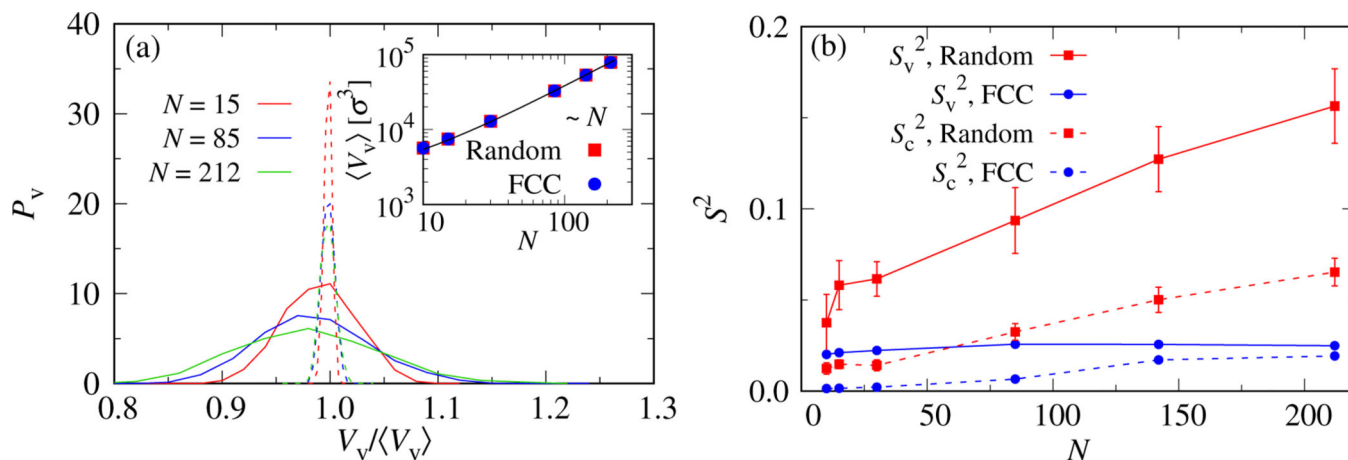
Figure 6:

(a) Normalized distributions of the volume of Voronoi cells, V_v, of selected GNP systems with $\rho_g = 0.47\sigma^{-2}$, as indicated. The x-axis is scaled with the mean volume of the Voronoi cells, $\langle V_v \rangle$. Solid colored curves show the results for simulations with random initial positions, whereas dashed curves represent the same quantity for GNP systems initialized on an FCC lattice (area under the curve normalized to 0.3 instead of unity for better visualization). The inset presents the average volume of Voronoi cells, $\langle V_v \rangle$, as a function of N. The solid black line shows $\langle V_v \rangle = (4/3)\pi R_{tot}^3$. (b) Asphericity parameter, S^2, of the Voronoi cells (S_v^2 solid curves) and of the polymer coronas of the GNPs (S_c^2 dashed curves) as a function of N at fixed $\rho_g = 0.47\sigma^{-2}$. Results from random and FCC lattice starting configurations are shown as red and blue curves, respectively.
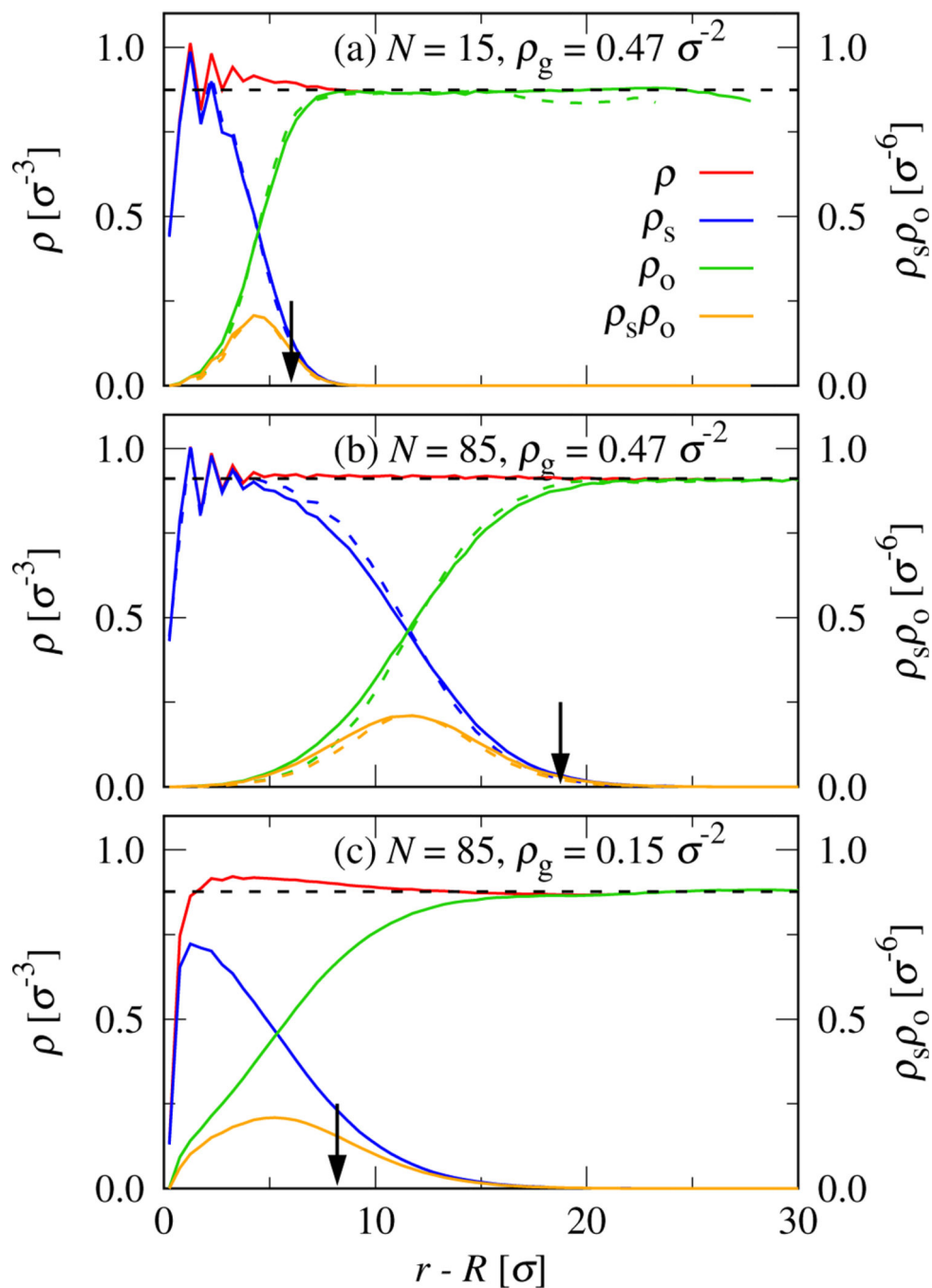
Figure 7:

Monomer density profiles of the grafted polymers around the NPs as a function of radial distance from the surface of the NPs, $r - R$, for various grafted chain lengths and grafting densities, (a) $N = 15$, $\rho_g = 0.47\sigma^{-2}$; (b) $N = 85$, $\rho_g = 0.47\sigma^{-2}$; and (c) $N = 85$, $\rho_g = 0.15\sigma^{-2}$. Here, ρ is the local monomer density, ρ_s is the monomer density of the chains coming from the central NP, and ρ_o is the monomer density from other GNPs. Interpenetration layers are quantified by the product of monomer density profiles, $\rho_s\rho_o$, which are represented by orange lines. Solid and dashed colored lines show the results for random and FCC starting

configuration, respectively. The horizontal black dashed line represents the average monomer density in the GNP systems. Black vertical arrows represent the average surface-to-surface distance between neighboring NPs, $r_{nn} - 2R$.
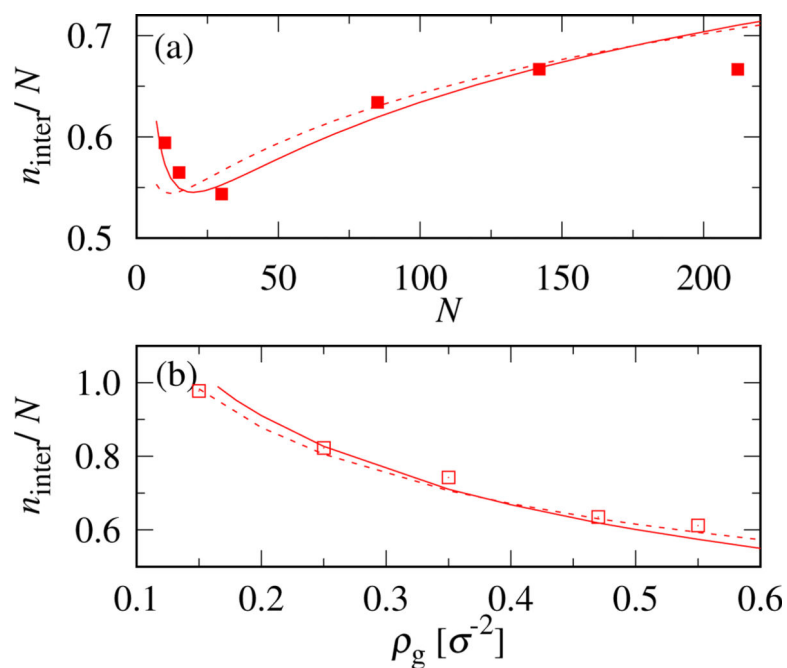
Figure 8:
Fraction of monomers in the interpenetration zone n_{inter}/N as a function of (a) N at fixed ρ_g = $0.47\sigma^{-2}$ and (b) ρ_g at fixed N = 85. The symbols show the simulation results (initialized from random NP locations) and the solid lines indicate the theoretical prediction from our two-layer model. The dashed lines are the theoretical predictions of the modified model of Kapnistos *et al.*[25]
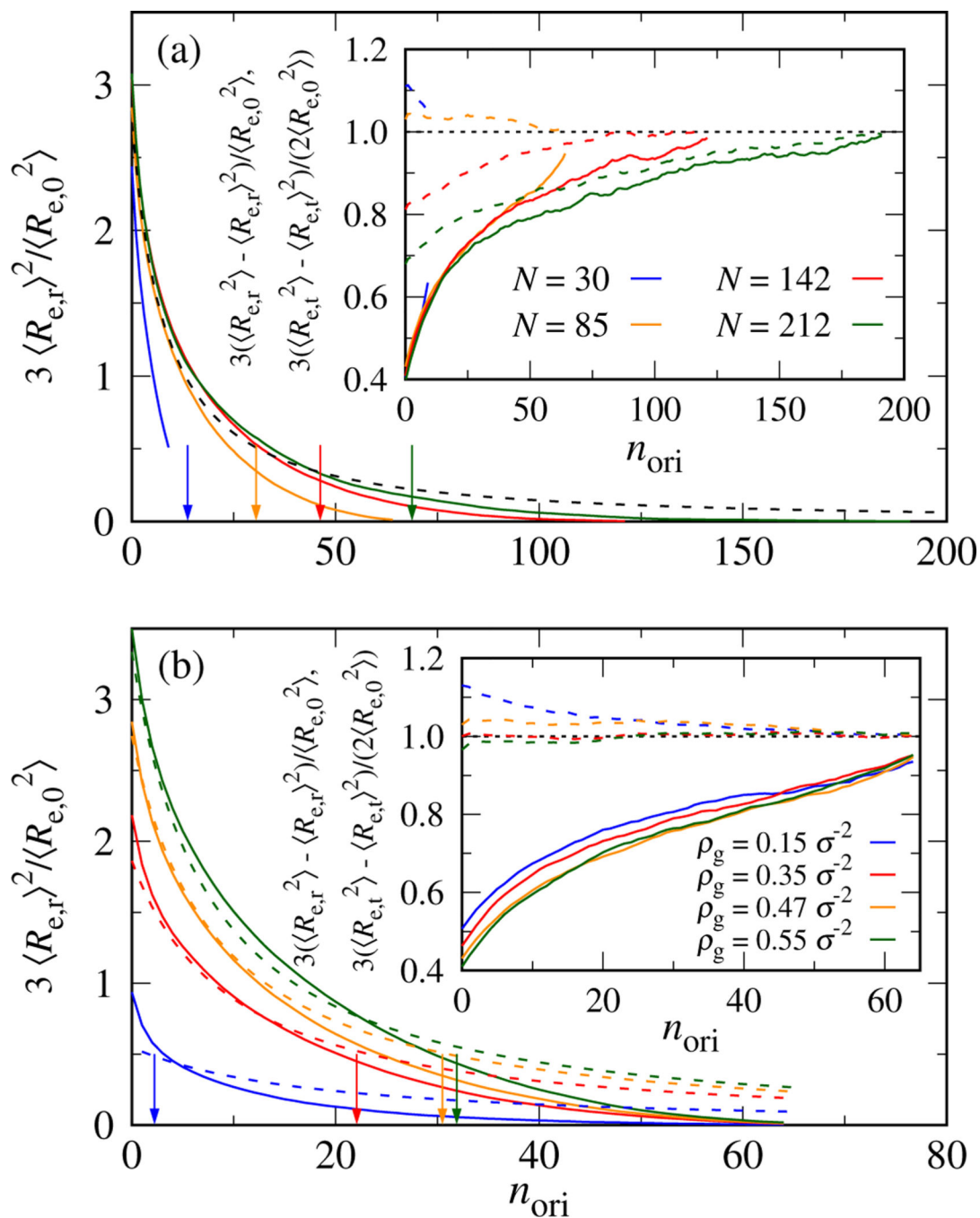
Figure 9:

Main plots: Square of normalized average radial end-to-end distances $3\langle R_{e,r}\rangle^2/\langle R_{e,0}^2\rangle$ in chain sections of length n. The dashed lines correspond to the theoretical prediction from our two-layer model $3[h(n_{ori}+n)-h(n_{ori})]^2/(nb^2)$, while vertical colored arrows indicate n_{dry} from our simulations. Insets: Normalized fluctuations of the radial (solid) and transverse (dashed) components of the end-to-end vector, $3(\langle R_{e,r}^2\rangle - \langle R_{e,r}\rangle^2)/\langle R_{e,0}^2\rangle$ and $3(\langle R_{e,t}^2\rangle - \langle R_{e,t}\rangle^2)/\langle R_{e,0}^2\rangle$, respectively. In all panels, the chain section length is fixed at $n =$

20 with one chain end at monomer n_{ori} and the other end at monomer $n_{ori} + n$. Data shown for GNP systems with (a) $N = 30, 85, 142$ and 212 at $\rho_g = 0.47\sigma^{-2}$, and (b) $\rho_g = 0.15\sigma^{-2}$, $0.35\sigma^{-2}$, $0.47\sigma^{-2}$, and $0.55\sigma^{-2}$ at $N = 85$.
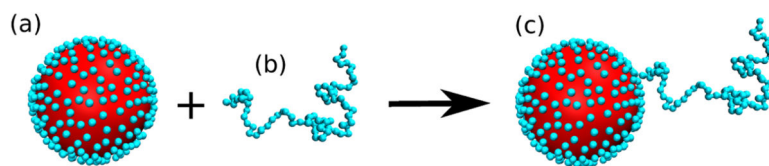
Figure 10:
Schematic of (a) an NP with all grafting beads, (b) a polymer chain which will be grafted to the NP surface, and (c) the resulting GNP with one grafted chain.

Table 1:

Brush thickness extracted from the average volume of Voronoi cells constructed around the NPs, $h_v = [3\langle V_v \rangle / (4\pi)]^{1/3} - R$; from the distance between nearest neighbors, $h_{nn} = r_{nn}/2 - R$; and from the peak position h_ρ of the product of the radial density profiles $\rho_s \rho_o$. The full width at half maximum δ of the product $\rho_s \rho_o$ is also shown. Results are included for random and FCC lattice starting configurations, as indicated.

N	$\rho_g\ [\sigma^{-2}]$	$h_v\ [\sigma]$	Random			FCC		
			$h_{nn}\ [\sigma]$	$h_\rho\ [\sigma]$	$\delta\ [\sigma]$	$h_{nn}\ [\sigma]$	$h_\rho\ [\sigma]$	$\delta\ [\sigma]$
10	0.47	3.6	2.3	3.4	2.7	2.5	3.4	2.6
15	0.47	4.6	3.2	4.4	3.3	3.3	4.4	3.0
30	0.47	7.0	5.1	6.7	4.5	5.7	6.8	4.2
85	0.47	12.4	9.1	11.5	8.2	10.4	11.6	7.1
142	0.47	15.9	12.0	14.7	10.6	13.7	15.0	8.8
212	0.47	19.3	14.5	17.7	12.3	16.6	18.1	10.0
85	0.15	6.6	4.0	5.3	9.1	-	-	-
85	0.25	8.8	6.1	7.8	8.8	-	-	-
85	0.35	10.7	7.8	9.6	8.8	-	-	-
85	0.55	13.4	9.9	12.4	8.7	-	-	-

Table 2:

Information about the simulated systems. Grafting density ρ_g, number of monomers per grafted chain N, overcrowding parameter x, number of NPs N_{NP}, total number of monomers in the system $\mathcal{N}$, average monomer density ρ, and packing fraction of NPs in the system ϕ_{NP}. Random and FCC lattice starting configurations led to the same values for ρ and ϕ_{NP} within our measurement accuracy.

$\rho_g\,[\sigma^{-2}]$	N	x	Random		FCC		$\rho\,[\sigma^{-3}]$	ϕ_{NP}
			N_{NP}	$\mathcal{N}$	N_{NP}	$\mathcal{N}$		
0.47	10	6.88	50	166,000	32	106,240	0.848	0.312
0.47	15	6.10	50	249,000	32	159,360	0.873	0.237
0.47	30	4.96	50	498,000	32	318,720	0.895	0.138
0.47	85	3.57	25	705,500	32	903,040	0.910	0.054
0.47	142	3.02	25	1,1786,00	32	1,508,608	0.914	0.033
0.47	212	2.65	25	1,759,600	32	2,252,288	0.916	0.023
0.15	85	1.65	50	450,500	–	–	0.877	0.147
0.25	85	2.33	40	598,400	–	–	0.897	0.096
0.35	85	2.93	32	671,480	–	–	0.906	0.071
0.55	85	3.97	20	659,600	–	–	0.913	0.047